Inorganic Chemistry
ARTICLE
pubs.acs.org/IC

Cation Distribution in Co-Doped $ZnAl_2O_4$ Nanoparticles Studied by X-ray Photoelectron Spectroscopy and ^{27}Al Solid-State NMR Spectroscopy

Xiulan Duan,* Duorong Yuan, and Fapeng Yu

State Key Laboratory of Crystal Materials, Shandong University, Jinan 250100, People's Republic of China

ABSTRACT: $Co_xZn_{1-x}Al_2O_4$ (x = 0.01−0.6) nanoparticles were synthesized by the citrate sol−gel method and were characterized by X-ray powder diffraction and transmission electron microscopy to identify the crystalline phase and determine the particle size. X-ray photoelectron spectroscopy and ^{27}Al solid-state NMR spectroscopy were used to study the distribution of the cations in the tetrahedral and octahedral sites in $Co_xZn_{1-x}Al_2O_4$ nanoparticles as a function of particle size and composition. The results show that all of the as-synthesized samples exhibit spinel-type single phase; the crystallite size of the samples is about 20−50 nm and increases with increasing annealing temperature and decreases with Co-enrichment. Zn^{2+} ions are located in large proportions in the tetrahedral sites and in small proportions in the octahedral sites in $Co_xZn_{1-x}Al_2O_4$ nanoparticles. The fraction of octahedral Zn^{2+} increases with increasing Co concentration and decreases with increasing particle size. Besides the tetrahedral and octahedral coordinations, the presence of the second octahedrally coordinated Al^{3+} ions is observed in the nanoparticles. The change of the inversion parameter (2 times the fraction of Al^{3+} ions in tetrahedral sites) with Co concentration and particle size is consistent with that of the Zn fraction in octahedral sites. Analysis of the absorption properties indicates that Co^{2+} ions are located in the tetrahedral sites as well as in the octahedral sites in the nanoparticles. The inversion degree of Co^{2+} decreases with increasing particle size.

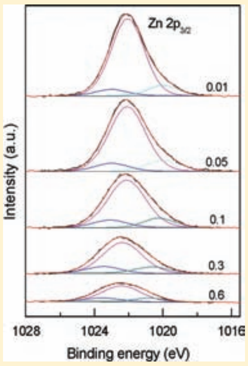

1. INTRODUCTION

Spinel-type oxides AB_2O_4, where A and B stand for divalent and trivalent metal cations, respectively, have a wide range of applications, such as catalyst, ceramic, magnetic, and host materials because of their good thermal and chemical stability.[1−4] The spinel structure is characterized by two types of cation sites: octahedral and tetrahedral. The distribution of A and B cations in these two sites, which is affected by the combination and nature of the two cations, depends strongly on the temperature, impurity content, and particle size.[5−8] The cation distribution can be characterized by the inversion parameter y, which is defined as the fraction of the divalent cations in octahedral sites (or 2 times the fraction of Al^{3+} ions in the tetrahedral sites). Taking into account the cation distribution, the general chemical formula of spinel can be written as $(A_{1-y}B_y)[A_yB_{2-y}]O_4$, where the parentheses () and brackets [] represent the tetrahedral and octahedral sites, respectively, and y denotes the inversion parameter. Studies of cation distribution in spinels have attracted much attention because they may allow better understanding of the correlations between structure and properties such as color, magnetic behavior, catalytic activity, and optical properties, etc., which are strongly dependent on the occupation of these two sites by metals.[9−12]

Among the class of materials, Co^{2+}-doped $ZnAl_2O_4$ and $MgAl_2O_4$ spinels have attracted much attention because they could be used as saturable absorber passive Q-switches for 1.34 and 1.54 μm lasers or be considered as possible candidates for tunable solid-state lasers in the visible and near-infrared.[13−19] Recently, they have been used as pigments.[20−23] Several methods have been employed for the synthesis of aluminate spinels, such as solid-state reaction,[24] coprecipitation,[25] sol−gel,[26] and hydrothermal method.[27] Previous studies showed that the cation inversion of pure $ZnAl_2O_4$ spinel was very low in samples with high crystallinity and its inversion degree increased with Co^{2+}-doping.[28−30] In 2009, Gaudon studied the structure feature of Co-doped $ZnAl_2O_4$ spinel as a function of synthesis temperature by Rietveld analyses and NMR.[23] The effect of particle size on the degree of distribution of Al and the inversion parameter of Co-doped $ZnAl_2O_4$ nanoparticles have not been studied so far.

In this study, we report a systematic study on the local structural variations in Co-doped $ZnAl_2O_4$ nanoparticles obtained by citrate sol−gel method as a function of particle size and composition by means of X-ray photoelectron spectroscopy (XPS) and ^{27}Al solid-state NMR spectroscopy. The UV−vis absorption spectra of the materials were studied, and the relationship between the structure and the optical properties was also discussed.

2. EXPERIMENTAL SECTION

Co-doped $ZnAl_2O_4$ nanoparticles with the theoretical composition of $Co_xZn_{1-x}Al_2O_4$ (x = 0.01−0.6) were synthesized by the sol−gel method using citric acid as a chelating agent. First, stoichiometeric $Co(NO_3)_2 \cdot 6H_2O$ (analytical reagent, A.R.), $Zn(NO_3)_2 \cdot 6H_2O$ (A.R.), and $Al(NO_3)_3 \cdot 9H_2O$ (A.R.) were dissolved in deionized water. Next, citric acid was added to the above solution with stirring. The molar ratio of metal ions to citric acid was 1:2. The mixed solution was stirred for 1 h and then heated in an 80 °C water bath until a highly viscous gel was

Received: December 7, 2010
Published: May 25, 2011

formed. The pink gels were dried in oven at 110 °C and then fired to the desired temperatures (500−1000 °C) for 5 h.

Powder X-ray diffraction (XRD) patterns of the samples were carried out on a Japan Rigaku D/Max-rA diffractometer using a Cu-target tube (λ = 0.15418 nm) and a graphite monochromator. The samples were step-scanned in steps of 0.016° (2θ) using a count time of 0.1 s/step.

Transmission electron microscopy (TEM) images of the Co-doped $ZnAl_2O_4$ nanoparticles were recorded with a JEM-100CXII transmission electron microscope. For the sample preparation, the powder was ultrasonicated in ethanol, and then a droplet of the suspension was deposited and dried on the sample support.

X-ray photoelectron spectra (XPS) were measured using a Thermofisher ESCALAB 250 X-ray photoelectron spectrometer with monochromatized Al K_α X-ray radiation in ultrahigh vacuum ($<10^{-7}$ Pa). The binding energies were calibrated by using the C1s peak (284.6 eV) of carbon impurities as a reference. The peaks were deconvoluted after background subtraction, using a mixed Gaussian−Lorentzian function. Fractional atomic concentrations of the elements were calculated using empirically derived atomic sensitivity factors.

^{27}Al solid-state NMR spectra were recorded at 104.2 MHz with a pulse width of 0.33 μs on a Bruker Avance 400 solid-state spectrometer by using an aluminum sulfate liquid solution as a reference. The spinning speed was 23 kHz using 3.2 mm zirconia rotors.

Diffuse absorbance spectra after Kubelka−Munk transformation were recorded with a step of 1 nm on a Varian Cary 5000 spectrophotometer using an integration sphere at room temperature. Polytetrafluoroethene was used as reference.

3. RESULTS AND DISCUSSION

3.1. Synthesis of $Co_xZn_{1-x}Al_2O_4$ Nanoparticles. To identify the crystalline phase and compare the particle size, X-ray powder diffraction (XRD) analyses were performed on the samples with various heat-treatment temperatures and different compositions. Figure 1a shows the powder XRD patterns of the $Co_{0.3}Zn_{0.7}Al_2O_4$ sample annealed at 500−1000 °C. It is noted that the sample annealed at 500 °C is amorphous. When the sample was heated to 550 °C, the XRD pattern exhibits several distinct broad diffraction peaks, indicating the nanocrystalline nature. The intensity of the peaks increases with increasing annealing temperature, indicating crystallite growth. All peaks indexed as (220), (311), (400), (331), (422), (511), (440), (620), and (533) crystal planes in the XRD patterns are assigned to cubic spinel phase according to the JCPDS nos. 5-669 and 10-458 for $ZnAl_2O_4$ and $CoAl_2O_4$, respectively. The average grain size of the samples annealed at different temperatures was calculated by means of the Scherrer formula: $D = 0.9\lambda/(\beta \cos \theta)$, where λ is the X-ray wavelength (0.15418 nm), β is the full width at half-maximum (fwhm) intensity of the diffraction line, and θ is the diffraction angle. The calculated average particle size is shown in Table 1. The $Co_{0.3}Zn_{0.7}Al_2O_4$ particles annealed at 600 °C (CZA1) and 800 °C (CZA2) have an average size of 25 and 28 nm, respectively, and the particles grow rapidly and increase to 42 nm when the heat-treatment temperature is up to 1000 °C.

The XRD patterns of the $Co_xZn_{1-x}Al_2O_4$ (x = 0.01−0.6) samples annealed at 800 °C are shown in Figure 1b. At this temperature for all of the values of x studied, only the characteristic peaks corresponding to the spinel phase are present (JCPDS nos. 5-669 and 10-458), and no secondary phases are detected.

On the basis of the XRD data, the values of lattice parameter and crystallite size of the $Co_xZn_{1-x}Al_2O_4$ nanoparticles as a function of composition were estimated, and the results are shown in Figure 2. As the cobalt fraction (x) increases from 0.01 to 0.6, the lattice parameter (a) increases from 8.081 to 8.090 (±0.001) Å, which is consistent with the literature data on $ZnAl_2O_4$ (a = 8.08 Å) and $CoAl_2O_4$ (a = 8.10 Å),[31,32] while the mean crystallite size decreases from 38 to 24 nm with the Co-enrichment of the samples. The results are similar to the previous studies.[21,22] The lattice parameter obeys Vegard's rule closely and increases linearly with the concentration of Co(x).

Figure 3 shows the TEM images of $Co_{0.3}Zn_{0.7}Al_2O_4$ nanoparticles annealed at 600−1000 °C. The image indicates an average particle diameter of 20−45 nm, which is consistent with the XRD analysis (25−42 nm). The particles tend to large agglomerate when heated above 900 °C.

Table 1. Sample Codes, Annealing Temperature, and Particle Sizes of the $Co_{0.3}Zn_{0.7}Al_2O_4$ Samples

sample code	annealing temperature (°C)	particle size (±1 nm) XRD	particle size (±1 nm) TEM
CZA1	600	25	20
CZA2	800	28	27
CZA3	900	36	38
CZA4	1000	42	45

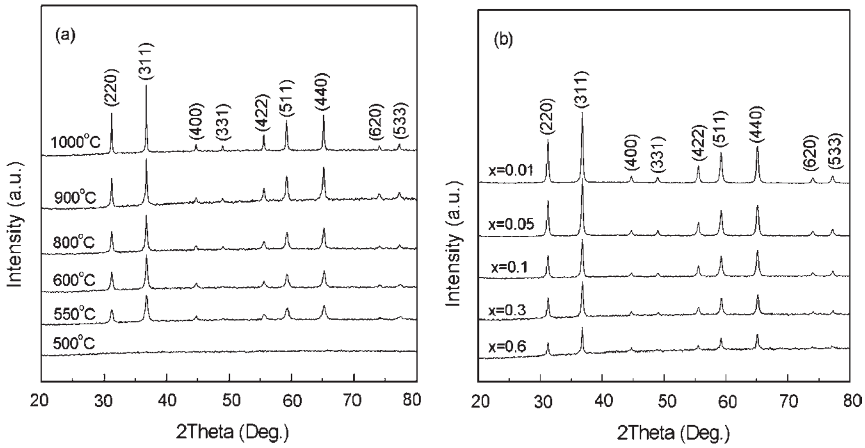

Figure 1. (a) XRD patterns of $Co_{0.3}Zn_{0.7}Al_2O_4$ sample calcined at different temperatures; (b) XRD patterns of $Co_xZn_{1-x}Al_2O_4$ (x = 0.01−0.6) nanoparticles calcined at 800 °C.

3.2. XPS Studies. We determined the survey XPS spectra of the 800 °C-annealed samples with the compositions of $Co_{0.05}Zn_{0.95}Al_2O_4$ and $Co_{0.3}Zn_{0.7}Al_2O_4$. The spectra indicate that no other elements were detected except for the original components and contaminated carbon (Figure 4). The C 1s peak at 284.6 eV of carbon contaminations was used as reference. To analyze the coordination of aluminum in the near-surface region, the high-resolution photoelectron spectra of Al 2p for the samples with different particle sizes and different compositions were measured, and the results are displayed in Figure 5a and b.

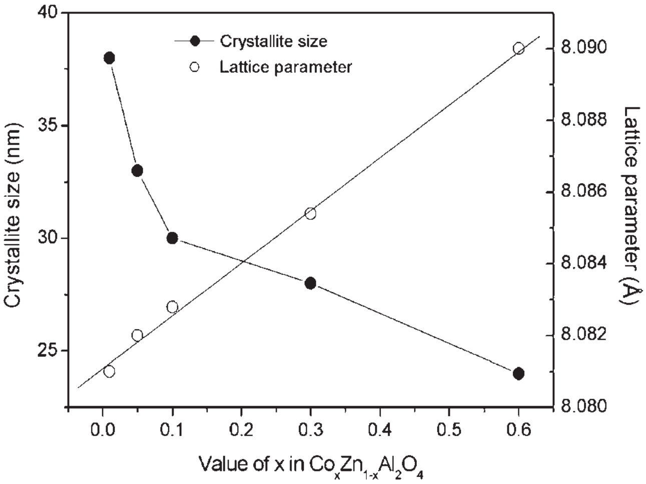

Figure 2. Crystallite size and lattice parameter of $Co_xZn_{1-x}Al_2O_4$ (x = 0.01, 0.05, 0.1, 0.3, 0.6) nanoparticles calcined at 800 °C as a function of the Co concentration.

In our experiment, all of the Al 2p spectra are relatively broad and asymmetric, which indicates that the Al^{3+} ions occupy more than one coordination environment in the samples. After deconvolution, Al 2p spectra are composed of two peaks. To make fitting results reliable, the positions of the two peaks are fixed at 74.3 and 73.0 eV for all of the Al 2p spectra in fitting process. The binding energy values of the two peaks are reasonable when compared to those of Al^{3+} ions in other materials,[36] as listed in Tables 2 and 3. The main peak at higher binding energy can be ascribed to Al^{3+} ions placed at the octahedral sites, and the Al 2p signal at the lower binding energy can be ascribed to the Al^{3+} ions located at the tetrahedral sites. Octahedral Al^{3+} ions are dominant in all of the studied samples. On the basis of the result, we think that the as-synthesized $Co_xZn_{1-x}Al_2O_4$ nanoparticles are partially inversed spinel-structure. The inversion parameter y can be estimated according to the area ratio of the two peaks, which correspond to the tetrahedral and octahedral Al^{3+} ions, respectively. It can be seen from Table 2 that the y value is 0.24 for $Co_{0.3}Zn_{0.7}Al_2O_4$ nanoparticles with the size of 25 nm and decreases to 0.09 when the particle size is increased to 42 nm. The result indicates that the coordination environment of Al in Co-doped $Zn_2Al_2O_4$ spinel changes with particle size when the particles are of nanometer size. The fraction of Al^{3+} ions in the tetrahedral sites decreases with increasing particle size.

The dependence of Al 2p XPS spectra on the composition is shown in Figure 5b. The intensity of the peak corresponding to the four-coordinated Al^{3+} ions increases with increasing cobalt content. The inversion parameter (y) increases from 0.10 to 0.21 as the cobalt fraction (x) increases from 0.01 to 0.6 (Table 3). The result shows that the composition also affects the cation distribution in spinel structure. The inversion degree increases with Co-enrichment in $Co_xZn_{1-x}Al_2O_4$ nanoparticles.

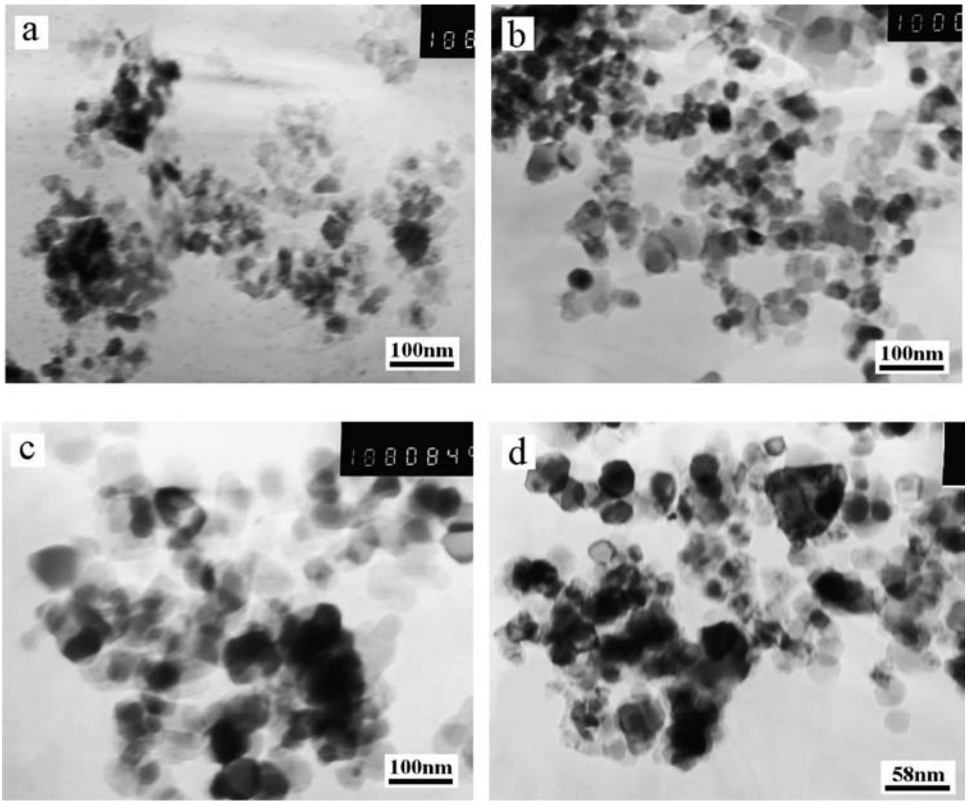

Figure 3. TEM images of $Co_{0.3}Zn_{0.7}Al_2O_4$ nanoparticles calcined at different temperatures: (a) 600 °C; (b) 800 °C; (c) 900 °C; (d) 1000 °C.

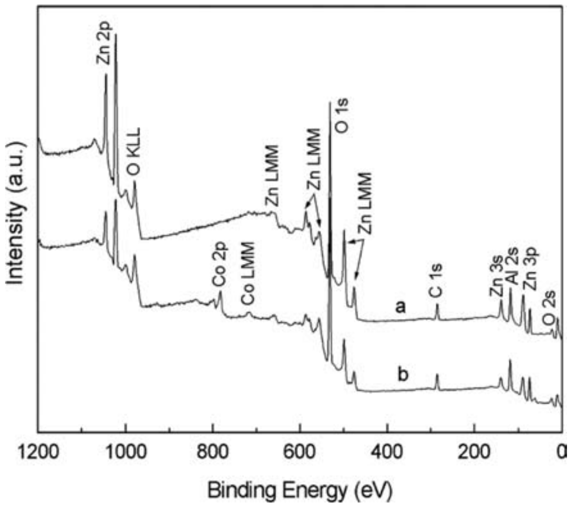

Figure 4. XPS survey spectra of (a) $Co_{0.01}Zn_{0.99}Al_2O_4$ and (b) $Co_{0.3}Zn_{0.7}Al_2O_4$ nanoparticles annealed at 800 °C.

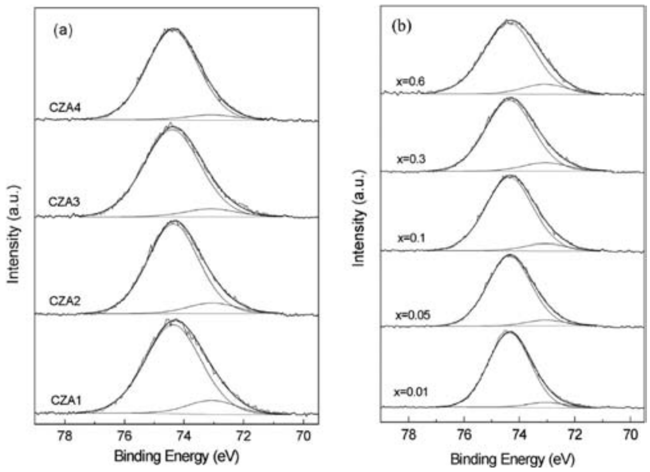

Figure 5. Al 2p XPS spectra of (a) $Co_{0.3}Zn_{0.7}Al_2O_4$ nanoparticles with different particle sizes; the sample codes are defined in Table 1. (b) $Co_xZn_{1-x}Al_2O_4$ (x = 0.01−0.6) nanoparticles annealed at 800 °C.

Table 2. XPS Data for Al 2p Spectra and Inversion Parameter (y) of $Co_{0.3}Zn_{0.7}Al_2O_4$ Nanoparticles with Different Particle Sizes

sample code	binding energy (±0.5%)	area percent (±0.1 eV)	fwhm (±0.1 eV)	y (±0.01)
CZA1	74.3	87.7	2.2	0.24
	73.0	12.3	2.0	
CZA2	74.3	90.1	2.1	0.19
	74.3	9.9	2.0	
CZA3	73.0	92.6	2.2	0.15
	73.0	7.4	2.1	
CZA4	74.3	95.3	2.1	0.09
	73.0	4.7	2.0	

Table 3. XPS Data for Al 2p Spectra and Inversion Parameter (y) of $Co_xZn_{1-x}Al_2O_4$ Nanoparticles Annealed at 800 °C

composition (x)	binding energy (±0.1 eV)	area percent (±0.5%)	fwhm (±0.1 eV)	y (±0.01)
0.01	74.3	94.9	1.8	0.10
	73.0	5.2	1.8	
0.05	74.3	93.9	1.9	0.12
	73.0	6.1	1.8	
0.1	74.3	91.8	2.0	0.16
	73.0	8.2	1.9	
0.3	74.3	90.1	2.2	0.19
	73.0	9.9	2.1	
0.6	74.3	89.3	2.2	0.21
	73.0	10.7	1.9	

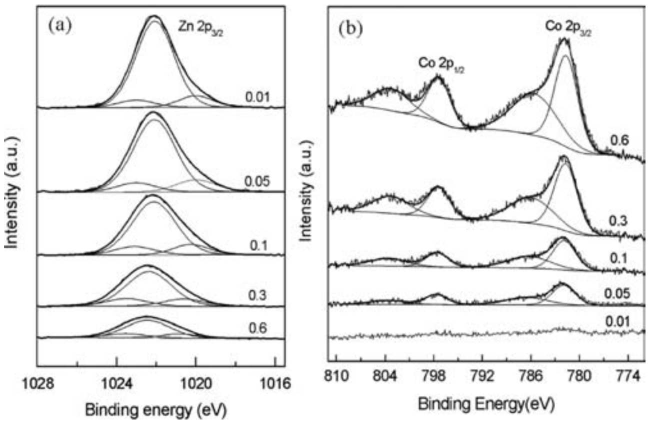

Figure 6. XPS spectra of (a) Zn 2p and (b) Co 2p core levels of $Co_xZn_{1-x}Al_2O_4$ (x = 0.01−0.6) nanoparticles annealed at 800 °C.

Table 4. XPS Data for Zn $2p_{3/2}$ Spectra of $Co_xZn_{1-x}Al_2O_4$ Nanoparticles Annealed at 800 °C

composition (x)	binding energy (±0.1 eV)	area percent (±0.5%)	fwhm (±0.1 eV)	fraction of octahedral Zn^{2+}
0.01	1023.0	7	2.3	0.07
	1022.0	93	2.3	
0.05	1023.0	10	2.6	0.10
	1022.1	90	2.4	
0.1	1023.1	13	2.7	0.13
	1022.1	87	2.4	
0.3	1023.4	16	2.8	0.16
	1022.3	84	2.5	
0.6	1023.5	18	2.8	0.18
	1022.4	82	2.6	

To study the chemical environments of divalent cations (Zn^{2+} and Co^{2+}) in samples, the high-resolution photoelectron spectra of Zn $2p_{3/2}$ and Co 2p core levels for the $Co_xZn_{1-x}Al_2O_4$ (x = 0.01−0.6) nanoparticles annealed at 800 °C were determined and shown in Figure 6a and b. The corresponding XPS data are shown in Tables 4 and 5.

According to the report by Druska in 1999, the Zn $2p_{3/2}$ binding energies of tetrahedral and octahedral Zn^{2+} ions are at

Table 5. Binding Energies of Co 2p Core Levels (in eV) of $Co_xZn_{1-x}Al_2O_4$ Nanoparticles Annealed at 800 °C

composition (x)	Co $2p_{3/2}$	Co $2p_{1/2}$
0.05	782.0	797.7
0.1	781.9	797.6
0.3	781.7	797.4
0.6	781.6	797.3

1021.0−1022.2 and 1022.9−1023.4 eV, respectively.[37] In our experiment, the Zn $2p_{3/2}$ spectra can be deconvoluted into three peaks. The peaks at about 1023 and 1022 eV can be assigned to octahedral and tetrahedral Zn^{2+} ions, respectively. The peak at ~1020 eV may be due to the impurities.[38] The fraction of octahedrally coordinated Zn^{2+} ions increases from 0.07 to 0.18 with the increasing of Co content from $x = 0.01$ to 0.6 (Figure 6a and Table 4).

The Co 2p XPS spectra of $Co_xZn_{1-x}Al_2O_4$ ($x \geq 0.05$) with different compositions show peaks at about 781.5 eV with the broad satellite around 786 eV, and 797.5 eV with the satellite around 803 eV, which are due to Co $2p_{3/2}$ and Co $2p_{1/2}$, respectively (Figure 6b). The Co $2p_{3/2}$ values are similar to those reported by Zsoldos (781.7 eV) and Chung (781.8 eV).[39,40] The peaks and their intense shakeup satellites are typical for divalent high spin cobalt.[41] However, the Co$2p_{3/2}$ peak with the fwhm of ~3.4 eV is rather broad. On the basis of the above analysis, the broad peak should arise from the distributions of Co^{2+} ions over tetrahedral and octahedral sites. The binding energy of Co$2p_{3/2}$ slightly decreases with increasing cobalt content, indicating that the relative amount of Co^{2+} ions in octahedral sites increases.

3.3. Al NMR Studies. Previous studies showed that the ^{27}Al NMR signal intensity decreases with increasing cobalt content due to the magnetic interactions between the paramagnetic Co^{2+} ions and the Al^{3+} ones.[23] In our studies, we determined the ^{27}Al NMR signals of the $Co_xZn_{1-x}Al_2O_4$ samples with $x \leq 0.01$ to study the dependence of Al coordination on particle size and composition. Figure 7a shows the ^{27}Al NMR spectra of $Co_{0.01}Zn_{0.99}Al_2O_4$ nanoparticles with different particle sizes. The ^{27}Al NMR signals of $Co_xZn_{1-x}Al_2O_4$ ($x = 0, 0.01$) samples annealed at 600 °C was shown in Figure 7b. For all of the samples, there are two main resonances observed in the range of 70−80 and 5−20 ppm. These two resonances correspond to Al in tetrahedral (Al_{IV}) and octahedral (Al_{VI}) sites, respectively. The Al_{VI} resonance peak appears as a doublet. Because ^{27}Al is a quadrupolar nucleus, its line shape is influenced by first- and second-order nuclear−quadrupole interactions, and the presence of the doublet stems from the second-order splitting of the central transition band by nuclear−quadrupole interaction. Furthermore, a slightly broadening is observed at the right-hand side of the Al_{VI} peak.

To estimate the relative concentration of Al in different coordination environments, all of the ^{27}Al NMR spectra have been deconvoluted by using the DMFIT computer program developed by Massiot et al.[42] The integrated intensities of each line and the relative intensities of the different coordination environments are calculated from the simulated spectra. Figure 7c and d shows the simulated spectra of $Co_{0.01}Zn_{0.99}Al_2O_4$ and $ZnAl_2O_4$ samples annealed at 600 °C, respectively. Besides the two resonances at 70−80 and 5−20 ppm, a new resonance peak at ~0 ppm is observed in the spectra and can be assigned to Al in a different octahedral site (Al_{VI-2}).

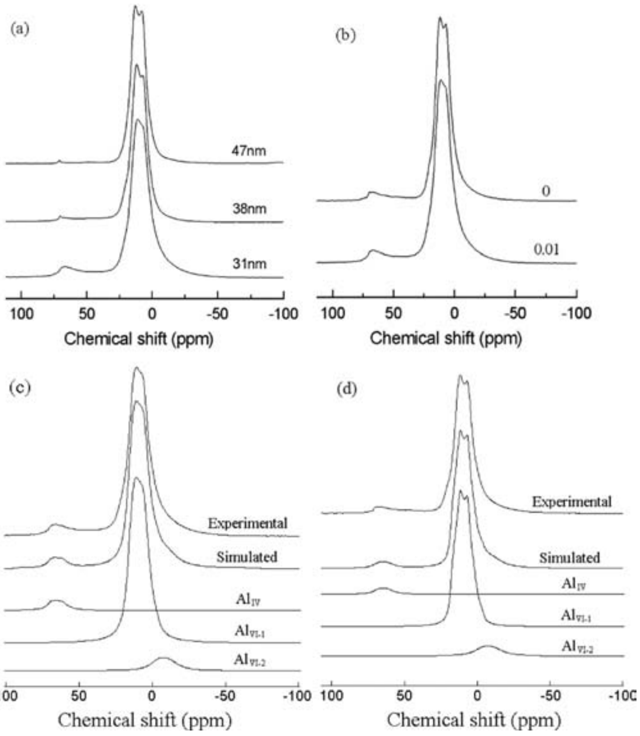

Figure 7. ^{27}Al MAS NMR spectra of (a) $Co_{0.01}Zn_{0.99}Al_2O_4$ nanoparticles with different particle sizes; (b) $Co_xZn_{1-x}Al_2O_4$ ($x = 0, 0.01$) nanoparticles annealed at 600 °C; and simulated ^{27}Al MAS NMR spectra of (c) $Co_{0.01}Zn_{0.99}Al_2O_4$ and (d) $ZnAl_2O_4$ nanoparticles annealed at 600 °C.

Correspondingly, the peak at 5−20 ppm due to octahedral Al is labeled as Al_{VI-1}. The fitted results are summarized in Tables 6 and 7. C_Q is the quadrupolar coupling constant. The inversion parameter was calculated according to the area percent of the peak corresponding to the tetrahedral Al^{3+} ions. From the fitted data, it can be seen that the relative amount of the tetrahedral Al decreases with increasing particle size and increases with Co-enrichment; the result is similar to the above XPS analysis.

From Tables 3 and 6, it can be seen that the inversion parameters obtained from XPS and NMR analyses are different for the same $Co_{0.01}Zn_{0.99}Al_2O_4$ nanoparticles annealed at 800 °C. The value calculated from XPS analysis (0.10) is higher than that calculated from NMR analysis (0.03). The difference may be due to the different region of analysis in the two techniques. XPS is predominantly a surface analytical technique, and the depth of information is approximately 3 nm for inorganic materials. So XPS shows the distribution of cations on surface, while NMR analysis predominantly reflects the distribution in the bulk of the samples. It is likely that most of the tetrahedral Al^{3+} ions come from the surface of the particles, and thereby the inversion parameter is higher for the surface than that for the bulk. The tetrahedral Al may be formed on the surface due to the existence of lots of oxygen vacancies. This assumption is further supported by the decreased contribution from the tetrahedral Al with increasing particle size (decreasing surface-to-volume).

The Al resonance peak at ~0 ppm has been also observed for the $ZnAl_2O_4$ and $MgAl_2O_4$ nanoparticles.[6,26] In ref 6, the authors thought that the Al_{VI-2} peak in the $MgAl_2O_4$ nanoparticles was likely due to local structural distortions in the octahedral sites in

Table 6. NMR Data for ^{27}Al NMR Spectra of $Co_{0.01}Zn_{0.99}Al_2O_4$ Nanoparticles with Different Particle Sizes

particle size (±1 nm)	annealing temperature (°C)	Al site	chemical shift (±0.1 ppm)	C_Q (±0.1 MHz)	area percent (±0.5%)	inversion parameter (±0.01
31	600	Al_{IV}	72.8	3.6	5.1	0.10
		$Al_{VI\text{-}1}$	17.9	3.7	85.3	
		$Al_{VI\text{-}2}$	0.8	3.8	9.6	
38	800	Al_{IV}	71.5	1.6	1.8	0.03
		$Al_{VI\text{-}1}$	17.8	3.6	94.4	
		$Al_{VI\text{-}2}$	0.8	3.1	3.8	
47	1000	Al_{IV}	71.6	1.1	0.2	0.01
		$Al_{VI\text{-}1}$	18.6	3.6	97.4	
		$Al_{VI\text{-}2}$	0.9	3.2	2.4	

Table 7. NMR Data for ^{27}Al NMR Spectra of $Co_xZn_{1-x}Al_2O_4$ (x = 0, 0.01) Nanoparticles Annealed at 600 °C

composition (x)	Al site	chemical shift (±0.1 ppm)	C_Q (±0.1 MHz)	area percent (±0.5%)	inversion parameter (±0.01)
0	Al_{IV}	71.7	3.5	4.2	0.08
	$Al_{VI\text{-}1}$	18.6	3.8	85.4	
	$Al_{VI\text{-}2}$	0.9	3.8	10.4	
0.01	Al_{IV}	72.8	3.6	5.1	0.10
	$Al_{VI\text{-}1}$	17.9	3.7	85.3	
	$Al_{VI\text{-}2}$	0.8	3.8	9.6	

the structure of spinel. This signal observed in our samples certainly corresponds to the same octahedral site, but is different due to structural distortions arising from the Co proximity in the Co-doped $ZnAl_2O_4$ nanoparticles.

3.4. Optical Properties. To study the correlation between the cation distribution and optical properties of Co-doped $ZnAl_2O_4$, the K/S absorption spectra were recorded in the wavelength range 250−800 nm. Figure 8 depicts the absorption spectra of the sample with the composition of $Co_{0.3}Zn_{0.7}Al_2O_4$ as a function of particle size. The sample with particle size of 42 nm (CZA4) shows an intense absorption peak at about 600 nm that gives the blue coloration of the samples. When the particle size decreases to 28 nm (CZA2), a broad absorption band at 300−500 nm appears in the spectrum. The intense peak at 600 nm, characteristic of Co^{2+} ions in tetrahedral sites in crystalline materials, is assigned to the $^4A_2(^4F) \rightarrow {}^4T_1(^4P)$ transition of tetrahedrally coordinated Co^{2+} ions.[14,33] With regard to the above discussions and the cation distribution previously characterized, the broad band at 300−500 nm, responsible for the green color, could be due to the Co^{2+} ions in octahedral sites. The similar band generated by octahedrally coordinated Co^{2+} ions has been reported by other authors.[34,35] With decreasing particle size, the intensity of the absorption band at 300−500 nm increases and the intensity of the peak at 600 nm decreases. This is because the fraction of the Co^{2+} ions in the octahedral sites is relatively large for the sample with relatively small particle size.

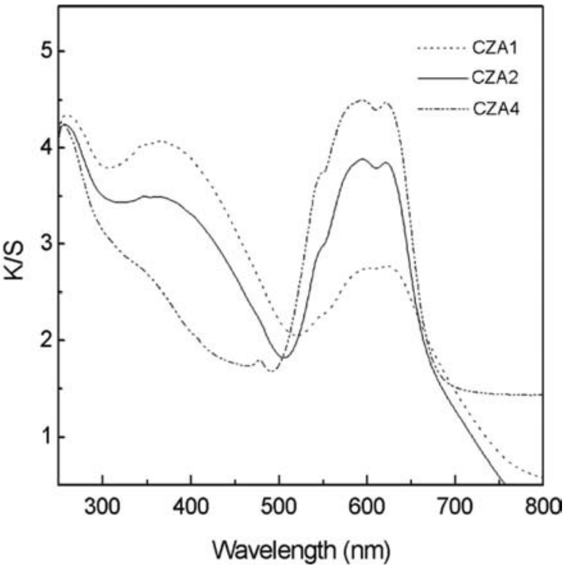

Figure 8. K/S absorption spectra of $Co_{0.3}Zn_{0.7}Al_2O_4$ nanoparticles as a function of particle size.

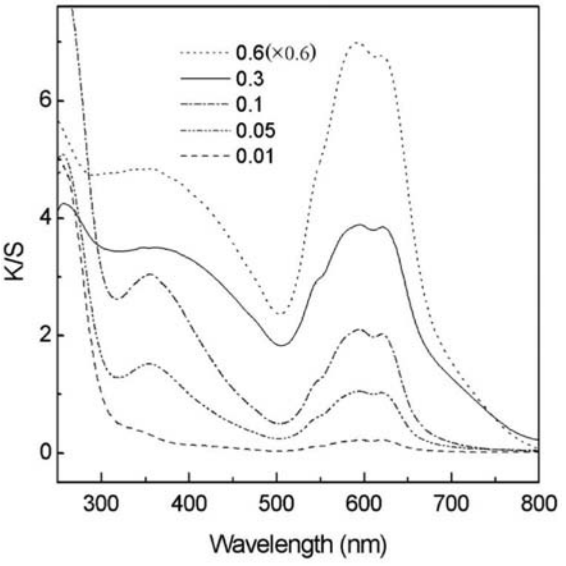

Figure 9. K/S absorption spectra of $Co_xZn_{1-x}Al_2O_4$ (x = 0.01−0.6) nanoparticles annealed at 800 °C.

The dependence of the absorption spectra of $Co_xZn_{1-x}Al_2O_4$ nanoparticles on the composition is shown in Figure 9. When the x value is 0.01, the spectrum exhibits a weak absorption peak centered at 600 nm. When the x value increases to 0.05, a new peak at about 350 nm is observed. The intensities of the two peaks, corresponding to tetrahedrally and octahedrally coordinated Co^{2+} ions, increase with increasing Co concentration. Furthermore, the absorption peak at about 350 nm becomes broad when $x \geq 0.3$. This is probably due to the fact that the concentration of cobalt in samples increases with increasing x value and the amount of Co in tetrahedral and octahedral sites increases.

The different absorption spectra of the samples may lead to their difference in color. The photographs of the samples with different Co concentrations are shown in Figure 10. The $Co_xZn_{1-x}Al_2O_4$ (x = 0.01) nanoparticles are light blue. The color of the samples with $x \geq 0.05$ is the mixture of blue and

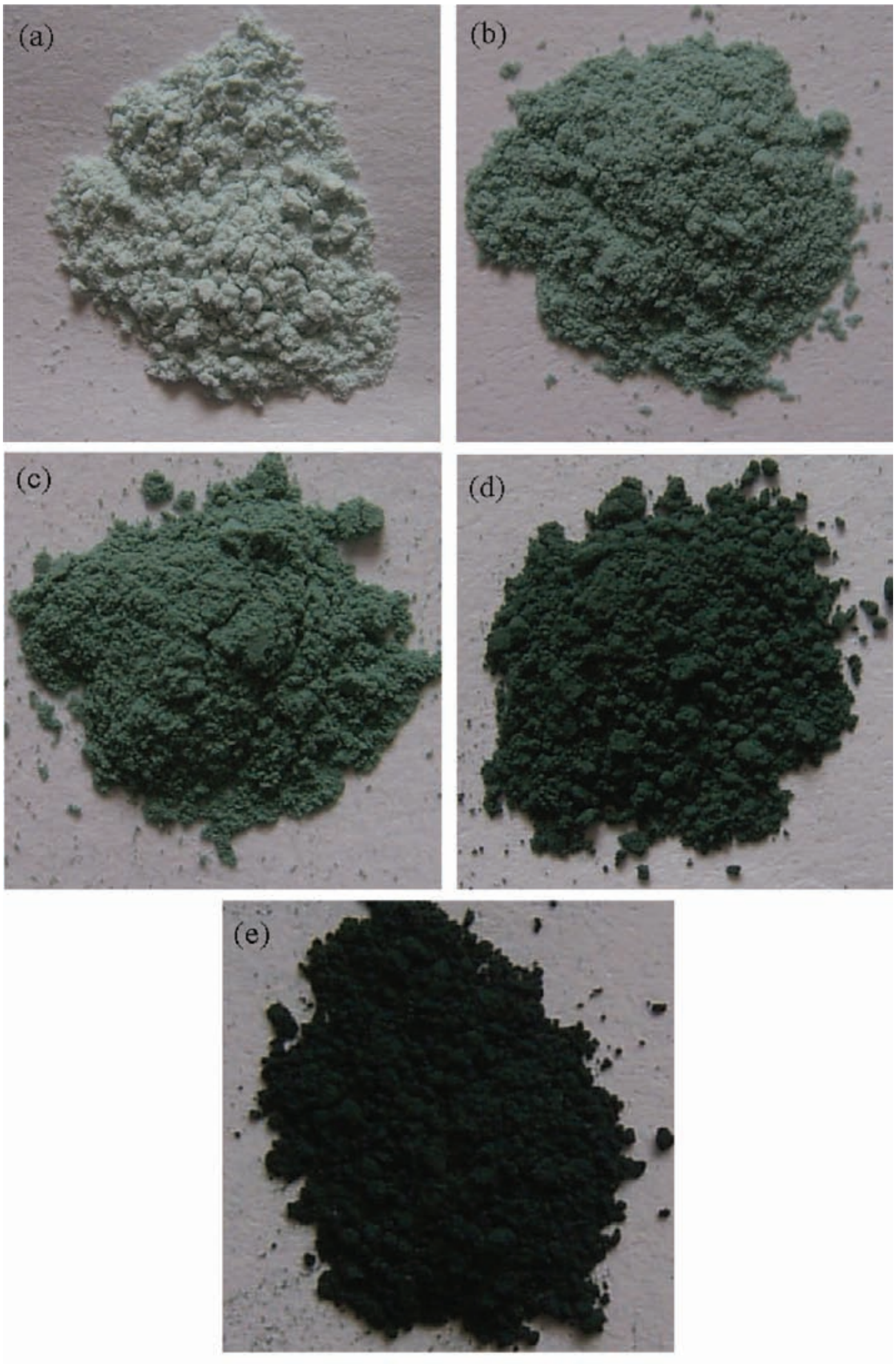

Figure 10. Photographs of the $Co_xZn_{1-x}Al_2O_4$ ($x = 0.01-0.6$) nanoparticles annealed at 800 °C.

green. The depth of the color increases with the Co enrichment in the samples.

4. CONCLUSIONS

Co-doped $ZnAl_2O_4$ nanoparticles were obtained by the sol−gel method using citric acid as a chelating agent. The effects of crystallite size and composition on the coordinative environments of the cations (Al^{3+}, Co^{2+}, and Zn^{2+} ions) have been investigated by XPS in combination with ^{27}Al NMR. It is shown that these cations are located not only in the octahedral sites but also in the tetrahedral sites in the studied samples. Apart from these two coordination environments, the second octahedrally coordinated Al^{3+} ions are observed in the NMR spectra. The tetrahedral Al^{3+} ions are likely to be located on the surface of the nanoparticles. The fraction of tetrahedral Al^{3+} ions increases with increasing cobalt content and decreases with increasing particle size. The zinc fraction in the octahedral sites varies in a similar way in comparison with tetrahedral aluminum ions. The optical properties of the nanoparticles are discussed on the basis of the structural results. The absorption band at 300−500 nm should be related to the octahedrally coordinated Co^{2+} ions. For a given composition, the fraction of Co^{2+} ions in the octahedral sites increases with decreasing particle size.

AUTHOR INFORMATION

Corresponding Author

*Phone: +86-531-88364864. Fax: +86-531-88364864. E-mail: xlduan@sdu.edu.cn.

ACKNOWLEDGMENT

This work was supported by grants from the National Natural Science Foundation of China (No. 50902089) and the Natural Science Foundation of Shandong Province (No. ZR2010EQ003).

REFERENCES

(1) Tielens, F.; Calatayud, M.; Franco, R.; Recio, J. M.; Perez-Ramirez, M.; Minot, C. *J. Phys. Chem. B* **2006**, *110*, 988–995.

(2) Ballarini, N.; Cavani, F.; Passeri, S.; Pesaresi, L.; Lee, A. F.; Wilson, K. *Appl. Catal., A* **2009**, *366*, 184–192.

(3) Sakavatu-Niasari, M.; Davar, F. *Mater. Lett.* **2009**, *63*, 441–443.

(4) Gul, I. H.; Maqsood, A.; Naeem, M.; Naeem Ashiq, M. *J. Alloys Compd.* **2010**, *507*, 201–206.

(5) Jovic, N. G.; Masadeh, A. S.; Kremenovic, A. S.; Antic, B. V.; Blanusa, J. L.; Cvjeticanin, N. D.; Goya, G. F.; Antisari, M. V.; Bozin, E. S. *J. Phys. Chem. C* **2009**, *113*, 20559–20567.

(6) Sreeja, V.; Smitha, T. S.; Nand, D.; Ajithkumar, T. G.; Joy, P. A. *J. Phys. Chem. C* **2008**, *112*, 14737–14744.

(7) Zhang, Z. J.; Wang, Z. L.; Chakoumakos, B. C.; Yin, J. S. *J. Am. Chem. Soc.* **1998**, *120*, 1800–1804.

(8) Mittal, V. K.; Chandramohan, P.; Bera, S.; Srinivasan, M. P.; Velmurugan, S.; Narasimhan, S. V. *Solid State Commun.* **2006**, *137*, 6–10.

(9) Pellerin, N.; Dodane-Thiriet, C.; Montouillout, V.; Beauvy, M.; Massiot, D. *J. Phys. Chem. B* **2007**, *111*, 12707–12714.

(10) Šepelák, V.; Indris, S.; Bergmann, I.; Feldhoff, A.; Becker, K. D.; Heitjans, P. *Solid State Ionics* **2006**, *177*, 2487–2490.

(11) Zou, L.; Xiang, X.; Wei, M.; Li, F.; Evans, D. G. *Inorg. Chem.* **2008**, *47*, 1361–1369.

(12) Le Nestour, A.; Gaudon, M.; Villeneuve, G.; Daturi, M.; Andriessen, R.; Demourgues, A. *Inorg. Chem.* **2007**, *46*, 4067–4078.

(13) Kuleshov, N. V.; Mikhailov, V. P.; Scherbitsky, V. G.; Prokoshin, P. V.; Yumashev, K. V. *J. Lumin.* **1993**, *55*, 265–269.

(14) Abritta, T.; Blak, F. H. *J. Lumin.* **1991**, *48&49*, 558–560.

(15) Camargo, M. B.; Stultz, R. D.; Birnbaum, M.; Kokta, M. *Opt. Lett.* **1995**, *20*, 339–341.

(16) Denisov, I. A.; Demchuk, M. L.; Kuleshov, N. V.; Yumashev, K. V. *Appl. Phys. Lett.* **2000**, *77*, 2455–2457.

(17) Yumashev, K. V. *Appl. Opt.* **1999**, *38*, 6343–6246.

(18) Malyarevich, A. M.; Denisov, I. A.; Yumashev, K. V.; Dymshits, O. S.; Zhilin, A. A.; Kang, U. *Appl. Opt.* **2001**, *40*, 4322–4325.

(19) Volk, Y. V.; Denisov, I. A.; Malyarevich, A. M.; Yumashev, K. V.; Dymshits, O. S.; Shashkin, A. V.; Zhilin, A. A.; Kang, U.; Lee, K. H. *Appl. Opt.* **2004**, *43*, 682–687.

(20) Ahmed, I. S.; Shama, S. A.; Moustafa, M. M.; Dessouki, H. A.; Ali, A. A. *Spectrochim. Acta, Part A* **2009**, *74*, 665–672.

(21) de Souza, L. K.C.; Zamiana, J. R.; Filhoa, G. N.; da, R.; Soledade, L. E. B.; dos Santos, I. M.G.; Souza, A. G.; Scheller, T.; Angelica, R. S.; da Costa, C. E. F. *Dyes Pigm.* **2009**, *81*, 187–192.

(22) Visinescu, D.; Paraschiv, C.; Ianculescu, A.; Jurca, B.; Vasile, B.; Carp, O. *Dyes Pigm.* **2010**, *87*, 125–131.

(23) Gaudon, M.; Apheceixborde, A.; Ménétrier, M.; Le Nestour, A.; Demourgues, A. *Inorg. Chem.* **2009**, *48*, 9085–9091.

(24) Le Nestour, A.; Gaudon, M.; Villeneuve, G.; Andriessen, R.; Demourgues, A. *Inorg. Chem.* **2009**, *46*, 2645–2658.

(25) Farhadi, S.; Panahandehjoo, S. *Appl. Catal., A* **2010**, *382*, 293–302.

(26) Da Silva, A. A.; Goncalves, A. D.; Davolos, M. R. *J. Sol-Gel Sci. Technol.* **2009**, *49*, 101–105.

(27) Chen, X. Y.; Ma, C. *Opt. Mater.* **2010**, *32*, 415–421.

(28) Van der Laag, N. J.; Snel, M. D.; Magusin, P. C. M. M.; de With, G. *J. Eur. Ceram. Soc.* **2004**, *24*, 2417–2424.

(29) O'Neill, H.; St., C.; Dollase, W. A. *Phys. Chem. Miner.* **1994**, *20*, 541–555.

(30) Jasminka, P.; EmiliJa, T.; BisErka, G.; Stanislav, K.; Boris, R. *Am. Mineral.* **2009**, *94*, 771–776.

(31) Christensen, A. N.; Norby, P.; Hanson, J. C. *Powder Diffr.* **1995**, *10*, 185–188.

(32) Garcia Casado, P.; Rasines, I. *J. Solid State Chem.* **1984**, *52*, 187–193.

(33) Ferguson, J.; Wood, D. L.; Van Uitert, L. G. *J. Chem. Phys.* **1969**, *51*, 2904–2910.

(34) Cava, S.; Tebcherani, S. M.; Pianaro, S. A.; Paskocimas, C. A.; Longo, E.; Varela, J. A. *Mater. Chem. Phys.* **2006**, *97*, 102–108.

(35) Matteucci, F.; Cruciani, G.; Dondi, M.; Gasparotto, G.; Tobaldi, D. M. *J. Solid State Chem.* **2007**, *180*, 3196–3210.

(36) Pawlak, D. A.; Woźniak, K.; Frukacz, Z.; Barr, T. L.; Fiorentino, D.; Seal, S. *J. Phys. Chem. B* **1999**, *103*, 1454–1461.

(37) Druska, P.; Steinike, U.; Šepelák, V. *J. Solid State Chem.* **1999**, *146*, 13–21.

(38) Tay, Y. Y.; Li, S.; Sun, C. Q.; Chen, P. *Appl. Phys. Lett.* **2006**, *88*, 173118.

(39) Zsoldos, Z.; Guczi, L. *J. Phys. Chem.* **1992**, *96*, 9393–9400.

(40) Chung, K. S.; Masslth, F. E. *J. Catal.* **1980**, *64*, 320–331.

(41) Briggs, D.; Seah, M. P. *Practical Surface Analysis*, 2nd ed.; Wiley: New York, 1993; Vol. 1.

(42) Massiot, D.; Fayon, F.; Capron, M.; King, I.; Calvé, S. L.; Alonso, B.; Durand, J. O.; Bujoli, B.; Gan, Z.; Hoatson, G. *Magn. Reson. Chem.* **2002**, *40*, 70–76.